Materialia 24 (2022) 101486

Contents lists available at ScienceDirect

Materialia

journal homepage: www.elsevier.com/locate/mtla

Electron channeling studies of atom site preference and distribution in doped $Mg_2Si_{1-x}Sn_x$ thermoelectrics

Andreas Delimitis[a,*], Theodora Kyratsi[b], Vidar Hansen[a]

[a] Department of Mechanical and Structural Engineering and Materials Science, University of Stavanger, Stavanger N-4036, Norway
[b] Department of Mechanical and Manufacturing Engineering, University of Cyprus, Nicosia CY-1678, Cyprus

ARTICLE INFO

Keywords:
Electron channeling
ALCHEMI
EDS
Atom site determination
Magnesium silicide thermoelectrics
doping

ABSTRACT

The electron channeling effect, i.e., the dependence of the characteristic x-ray emission on the crystallographic direction of the incoming beam in an analytical transmission electron microscope was employed to elucidate the crystal site location and distribution of the dopant and host ions in $Mg_2Si_{1-x}Sn_x$ thermoelectric (TE) materials, doped with low amounts of Bi. Experiments performed both in pure Bi-doped Mg_2Si and mixed $Mg_2Si_{1-x}Sn_x$ (x = 0.4, 0.6), firmly confirmed that Mg occupies the two tetrahedral T sites, 8c ($\frac{1}{4}$, $\frac{1}{4}$, $\frac{1}{4}$) and ($\frac{1}{4}$, $\frac{1}{4}$, $\frac{3}{4}$), with some vacancies present, too, whereas Si and Sn the 4a (0, 0, 0) and 4b ($\frac{1}{2}$, $\frac{1}{2}$, $\frac{1}{2}$) octahedral C and N sites, respectively. Bi ions follow the trend of Si and Sn, occupying 4a sites, but also there is a partial distribution of them in 4b sites. We moreover observe a certain degree of asymmetry along the {111} directions in $Mg_2Si_{1-x}Sn_x$, predominately for the variable distribution of Bi and Sn in the lattice, which indicates Bi substitution for Sn in an uneven fashion. The channeling results are in line with TE property measurements, especially in relation to lower thermal conductivity and negative Seebeck coefficient due to Bi incorporation in the lattice. These findings demonstrate once more the effectiveness of the channeling technique to provide direct crystallographic information and refine atom positions in materials, particularly for nanoscale crystal grains.

1. Introduction

Detailed structure studies by electron microscopy methods have been widely exploited due to the unique capabilities electrons provide. Precise identification of atom positions is feasible by employing spectroscopy techniques in an analytical transmission electron microscope. In this aspect, methods such as energy dispersive X-ray spectroscopy (EDS) or electron energy loss spectroscopy are utilised, under strong channeling conditions, where the yield of element characteristic X-ray emission can be modified and manipulated, dependent upon crystallographic directions of the incident beam [1]. These channeling effects are powerful in determining atomic site locations in crystals and techniques such as ALCHEMI (Atom Location by CHanneling Enhanced MIcroanalysis) have been developed and evaluated.

The non-uniformity in the intensity distribution of the incident electron beam over the projected unit cell of a given structure causes anomalous absorption effects and crystallographic direction-dependent X-ray emission, i.e., electron channeling phenomena. In addition, channeling is further enhanced by the localization of X-ray production sources at the proximity of the atom cores of the structure. Theoretical calculations [2] of the X-ray production rate $N_z(\boldsymbol{k}_i)$ by an element in the projected unit cell at a distance z from the entrance surface and for an incident beam direction $\boldsymbol{k}_i$, provide:

$$N_z(\boldsymbol{k}_\mathbf{i}) \approx \sum_l \int_0^t I(\boldsymbol{k}_\mathbf{i}, \boldsymbol{r}_\mathbf{i}, z)\rho_t dz \tag{1}$$

where ρ_t is the site occupancy at coordinate $\boldsymbol{r}_i$ and $I(\boldsymbol{k}_i,\boldsymbol{r}_l,z)$ is the intensity distribution of the electron beam. For the latter, calculation is performed using the Bloch waves approximation $b^j(\boldsymbol{r})$, so the intensity becomes:

$$I(\boldsymbol{k}_\mathbf{i}, \boldsymbol{r}_\mathbf{i}, z) = \sum_j \left|C_0^j\right|^2 \left|b^j(\boldsymbol{r})\right|^2 = \sum_j \left|C_0^j\right|^2 \left|\sum_g C_g^j \exp(2\pi \boldsymbol{g}\cdot\boldsymbol{r})\right|^2 \tag{2}$$

with g reciprocal lattice vectors, C_g^j Bloch wave coefficients and C_0^j the excitation strength of the jth Bloch wave at the entrance surface of the crystal unit cell. In order to facilitate calculations, the two beam approximation is used [3] where two Bloch waves are excited. In a planar case channeling experiment, where all atomic planes are equidistant and identical, one Bloch wave would be concentrated at the atomic planes, whereas the other Bloch wave midway between them, when the 1st order reflection is in Bragg. For negative excitation error, the atomic planes Bloch wave is strongly excited, whereas the opposite takes place

* Corresponding author.
E-mail address: andreas.delimitis@uis.no (A. Delimitis).

https://doi.org/10.1016/j.mtla.2022.101486
Received 23 February 2022; Accepted 19 June 2022
Available online 29 June 2022

for positive excitation error. In practise, in planar channeling experiments, Bragg scattering from only one family of crystal planes takes place. Then the projected structure is aligned with respect to the incident beam so that each plane contains only one kind of element in the structure.

Structural analyses employing electron channeling have a recent focus in systems for renewable technologies and energy harvesting, such as thermoelectric (TE) materials that convert waste heat into electricity. This energy conversion efficiency of TE devices is expressed by the dimensionless figure of merit ZT

$$ZT = S^2\sigma T/\kappa \quad (3)$$

where S is the Seebeck coefficient, σ the electrical conductivity, $\kappa = \kappa_l + \kappa_e$ the total thermal conductivity, comprising of its lattice (κ_l) and electronic (κ_e) counterparts and T the absolute temperature. Strategies towards improvement of ZT values over the last years aim to enhancing the power factor ($S^2\sigma$), and/or minimizing the thermal conductivity, either by band engineering, hierarchical architecturing, or endotaxial nanostructures [4], among others.

Electron channeling and ALCHEMI have been already proved quite efficient in providing essential structural refinement information [5,6] for half-Heusler compounds with basic TEM instrumentation requirements, the latter considered among the most promising TE materials [7],. However, its applicability can be readily extended to a wide range of TEs, such as ternary tellurides [8], higher Mn silicides [9], or mixed $Bi_2{\times}_3$ (X = Te, Se) ones [10]. Taking into account that recent developments in TEs involve flexible and environmental friendly approaches [11] or polycrystalline materials [12], the necessity of determination of the precise structural characteristics and their role in TE performance becomes crucial. Furthermore, its ease of applicability can render channeling an efficient complementary method for structural analysis, along with large scale characterization methods, such as synchrotron X-ray [13] or neutron diffraction.

TE materials based on mixed Mg_2Si - Mg_2Sn have gained increased interest, due to inexpensive production costs, abundancy and atoxic nature of raw starting powders, especially for power generation applications within the intermediate temperature range (500–900 K) [14]. Synthesis of $Mg_2Si_{1-x}Sn_x$ in nanocrystal morphologies, often coupled by incorporation of n-type dopants in their host matrix -Sb [15] or Bi [16]- is exploited, with a scope to efficiently increase electrical conductivity σ and reduce, at the same time, lattice thermal conductivity κ_l, particularly for Sn-rich or Bi doped Si-rich counterparts. In this way, the energy conversion efficiency of TE devices, i.e., the figure of merit ZT, will be significantly improved.

Previous studies [15] confirmed the multiplicity of phases in this system, such as Si-, Ge- and/or Sn-rich phases, where the distribution of the group IV ions in the unit cell may significantly differ [17,18]. Along with this, the exact location or distribution of dopants is also a controversial issue. In [19], Bi doping resulted in preferential segregation at grain boundaries, where it acts as a donor. In other works [20], Bi has shown to homogenously distributed in Mg_2Si. All these have significant effects in the TE properties. In particular, the thermal conductivity decreases, as scattering by point defects induced by dopants and/or misplacement of host ions decreases the contribution of short-wavelength phonons [17], thus resulting in improved TE properties. It also affects the n- or p-type electrical conductivity, as in [21], where ionized impurities in Mg_2Si-Mg_2Sn solid solutions affect carrier scattering at low temperatures: the same is also addressed in [22], for Sb doping ions.

Application of the electron channeling method is therefore highly beneficial in order to accurately determine and refine the structural characteristics of the $Mg_2Si_{1-x}Sn_x$ materials. In previous studies [5], electron channeling and the ALCHEMI technique have been employed for structure refinement of TE materials. ALCHEMI is capable to calculate the amount of dopants in TEs and may efficiently act as a complementary method to other techniques [22] to determine the level of doping for Sb dopants, for instance, showing to be up to 2.3 at% inside $Mg_2Si_{0.4}Sn_{0.6}$. In other works [23], the Mg vacancies are considered in $Mg_2Si_{1-x}Sn_x$ materials, as a consequence of increased (>10%) Sb incorporation in the lattice, to account for charge balance. The Mg vacancies and their interplay with Sb doping have been also investigated in [24], for $Mg_2Si_{0.4}Sn_{0.6-x}Sb_x$ with high Sb content (>10%). The Mg interstitials and vacancies are also associated with the n- or p-type conductivity of Mg_2Si in [25] and, although Mg vacancies are less energetically favoured, they should be present in Mg_2Si, based on experimental findings. Mg interstitials were found to occupy 4b ($\frac{1}{2}$, $\frac{1}{2}$, $\frac{1}{2}$) sites in [26]. Zwolenski et al. [27] also deals with Mg and Si ions at 4b interstitial sites, too; the authors there claim that, although the Si vacancy is more favoured at Mg_2Si, the Mg vacancy is more preferred at Mg_2Sn, whereas Mg_2Ge shows somehow intermediate behavior.

Table 1
Nominal contents of host and dopant atoms at the various Mg silicide samples.

Sample	Chemical formula	Mg	Si	Sn	Bi
Pure	Mg_2Si	2	0.97	0	0.03
Si-rich	$Mg_2Si_{0.57}Sn_{0.4}$	2	0.57	0.40	0.03
Sn-rich	$Mg_2Si_{0.38}Sn_{0.6}$	2	0.38	0.6	0.02

The unit cell site preference for both host and doping elements and the spatial variations in compositions are essential to understand the fundamental TE properties, such as electrical conductivity, Seebeck coefficient and the lattice contribution in thermal conductivity of Mg silicides [17]. In this study, we determine the host and dopant site preferences and distribution for Bi-doped $Mg_2Si_{1-x}Sn_x$ compounds (x = 0, 0.4, 0.6) employing the electron channeling method. In practice, the ALCHEMI technique is also applied to calculate and determine the percentage of Bi dopant ions in the pure and mixed $Mg_2Si_{1-x}Sn_x$ compounds. The results are compared and assessed in relation to the TE property measurements of the materials.

2. Materials and methods

2.1. Synthesis of silicides

Bi-doped $Mg_2Si_{1-x}Sn_x$ (x = 0, 0.4 and 0.6) materials were prepared by solid state reaction combined with ball milling and followed by hot press sintering as described in [15]. Magnesium (Mg), silicon (Si), tin (Sn) and bismuth (Bi) powders/chunks with purities higher than 99.8% (Alfa Aesar) were weighted according to the desired composition, as in Table 1.

2.2. TEM sample preparation and experimental details

Samples suitable for electron channeling analysis at the TEM were prepared by dissolving finely crushed material in high purity ethanol and evenly dispersing it on ultrathin lacey C-films supported on 3.05 mm copper grids. Electron channeling experiments were carried out on a JEOL 2100 transmission electron microscope (TEM) with a LaB_6 electron source, operating at 200 kV and with a point resolution of 0.25 nm. The TEM is fitted with an EDAX Apollo XLT silicon drift EDS detector, with an ultra-thin window and an energy resolution of 129 eV (Mn K). Spectrum acquisition and analysis was performed by the TEAM EDS Suite software.

2.3. Electron channeling

Mg_2Si-based compounds crystallize at the high symmetry $Fm\bar{3}m$ space group (#225), comprising of four interpenetrating fcc sublattices. In principle, at an ideal unit cell, Si, (or Sn or Ge) atoms occupy the octahedral 4a (0,0,0) sites (C sites), whereas Mg ones occupy the two tetrahedral 8c sites, ($\frac{1}{4}$, $\frac{1}{4}$, $\frac{1}{4}$) and ($\frac{1}{4}$, $\frac{1}{4}$, $\frac{3}{4}$) (T sites). There is also an

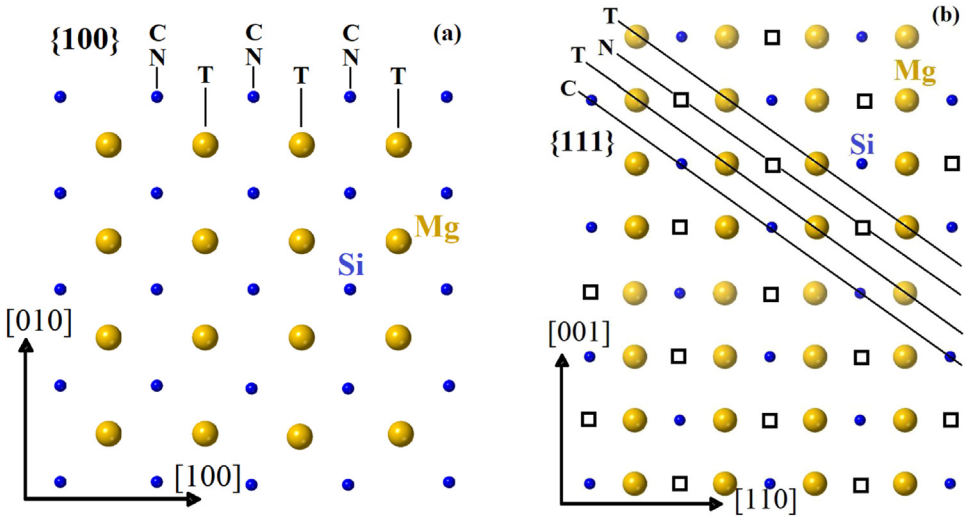

Fig. 1. The crystal structure of magnesium silicides, as viewed along the (a) [001] and (b) [1$\bar{1}$0] projections. The different sites are denoted with the letters T (tetrahedral), C and N (both octahedral); vacancies are also designated by open squares. Along the [111] direction, all sites are clearly distinguished, as shown by their …-C-T-N-T-… succession.

additional octahedral site at the unit cell, the 4b ($\frac{1}{2}$, $\frac{1}{2}$, $\frac{1}{2}$), i.e., N site that is, by principle, unoccupied. The crystal structure of Mg_2Si, viewed along the [001] and [1$\bar{1}$0] directions, is shown at Fig. 1. The two octahedral sites (i.e., the C and N ones) cannot be distinguished at the [001] projection, whereas all three different sites (C, N and T) can be easily distinguished along [1$\bar{1}$0], across, e.g., the {111} types of crystal planes, as shown in Fig. 1(b).

Furthermore, Fig. 1 also illustrates that there is an inversion symmetry across the (111) planes for the Mg_2Si compounds, as the sequence is …-C-T-N-T-C-, i.e., symmetric with respect to N sites. This is also confirmed by the expression of structure factor [28]

$$\boldsymbol{F}_{\mathbf{g}} = \boldsymbol{F}_{hkl} = \sum_i f_i \exp\left(2\pi \boldsymbol{g} \cdot \boldsymbol{r}_{\mathbf{i}}\right) \tag{4}$$

for all possible types of reflections:

Reflections with h, k, l even numbers have two subcategories:

- h + k + l = 4n, n ≥ 1, such as 220, 400, 440, etc., where

$$F_{hkl} = 4\left(f_C + f_N + 2f_T\right) \tag{5}$$

- h + k + l = 4n+2, n ≥ 0, such as 200, 222, 442, etc., where

$$F_{hkl} = 4\left(f_C + f_N - 2f_T\right) \tag{6}$$

For reflections with h, k, l odd numbers, such as 111, 311, 511, etc., the structure factor becomes:

$$F_{hkl} = 4\left(f_C - f_N\right) \tag{7}$$

i.e., it is interestingly only dependent on the occupancy of the C and N octahedral sites. This is a mere consequence of the high symmetry of the Mg_2Si structure and the full occupancy of both types of tetrahedral T sites by Mg ions at the unit cell.

Electron channeling experiments have been performed with a convergent beam of electrons focused on a thin area of interest [5], with a scope to avoid overlap between the diffraction disks at convergent beam electron diffraction (CBED) mode. Thus the probe size during analysis was set at ~40 nm and the beam semi-convergence angle was around 1.5 mrad. In the planar channeling experiment configurations employed in this study the {100} and {111} reciprocal lattice rows of reflections have been chosen. A typical set of CBED patterns for the {111} series is shown at Fig. 2, where the excitation of all reflections spanning the range from $\bar{4}\bar{4}\bar{4}$ to 444 are shown in successive order. Their corresponding Kikuchi lines help as a guide for the specific diffraction conditions

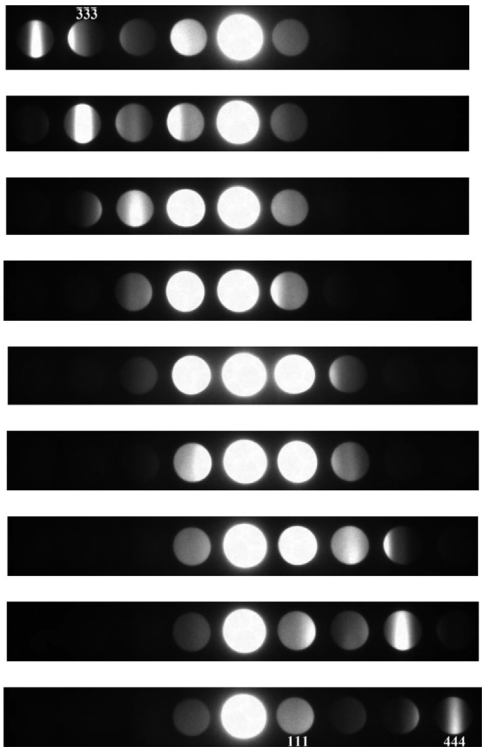

Fig. 2. Series of CBED patterns acquired during a typical {111}-series channeling experiment. Typical diffraction conditions are denoted at the patterns.

for each tilting angle. The optimum thickness of the areas being analyzed should, in principle, be less than 50% of the extinction distance for a specific reflection, i.e., usually in the range of 50–100 nm. Post-experimental fitting of all data was achieved by employing the *curve_fit()* function provided by the Python *SciPy* library.

3. Results and discussion

3.1. Pure Mg_2Si sample, doped with Bi

Fig. 3 shows a bright field (BF) TEM image of a typical area for channeling analysis in the pure Mg_2Si sample, doped with 3 at% Bi, along with its corresponding Selected Area Diffraction (SAD) pattern oriented

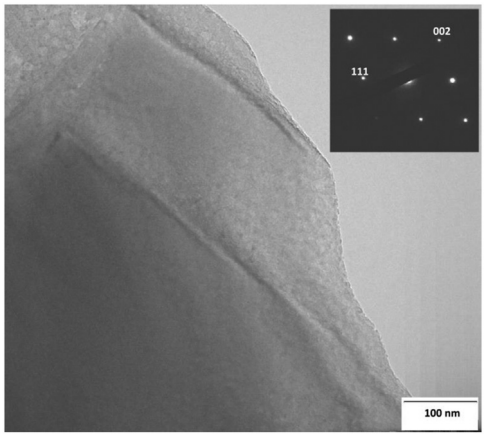

Fig. 3. BF image of a typical region for the channeling experiments at Mg_2Si, along with its SAD pattern inset, revealing the [1$\bar{1}$0] projection.

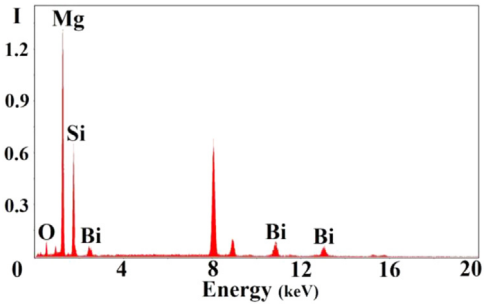

Fig. 4. Typical EDS spectrum from the pure Mg_2Si sample. The peaks at ~8 keV are the Cu K_α and K_β ones, stemming from the Cu grid used for the TEM sample preparation.

nearly along its [1$\bar{1}$0] zone axis. The Mg_2Si particle is crystalline and quite thin, thus highly suitable for the channeling experiments. Typical sizes of particles are up to 500 nm for this material. The SAD pattern further confirms that the particles in this study crystallize in the anti-fluorite Mg_2Si structure. It should be emphasized that the specific [1$\bar{1}$0] particle orientation was merely used for phase and crystalline quality confirmation and not as a starting point for orienting the particle during the channeling experiments.

A characteristic Energy Dispersive X-ray Spectrum (EDS) from the pure Mg_2Si is also shown in Fig. 4. The spectrum shows the Mg K and Si K peaks, along with the Bi L and M ones. EDS point analysis acquired from several areas of the same Mg_2Si particle confirmed the compositional uniformity, with the Mg, Si and Bi contents to be consistent, in general. For reasons of accuracy, we mainly relied on point analysis instead of elemental mapping options. EDS spectra did not reveal any other impurity peaks, apart from a small amount of O, attributed to some residual MgO phase formation that is commonly encountered in magnesium silicide compounds [15]. In certain cases, this additional MgO phase resulted in slight deviations from the nominal stoichiometry between Mg and Si, especially towards a deficiency in Mg trend, equal to 5–8%, in agreement with previous studies [15,25]. In addition, the Bi doping level varied slightly from its theoretical value among various particles, being about 2–2.5 at% on average. As no distinct Bi phases were detected, its slightly lower concentration in the Mg_2Si particles may well imply some segregation at grain boundaries, in accordance with previous reports [19].

Planar electron channeling experiments took place in typical Mg_2Si particles along the {100} and {111} rows of reflections and the results are presented in Figs. 5 and 6, respectively. There, the variation of the normalized X-ray emission as a function of angle between the incident

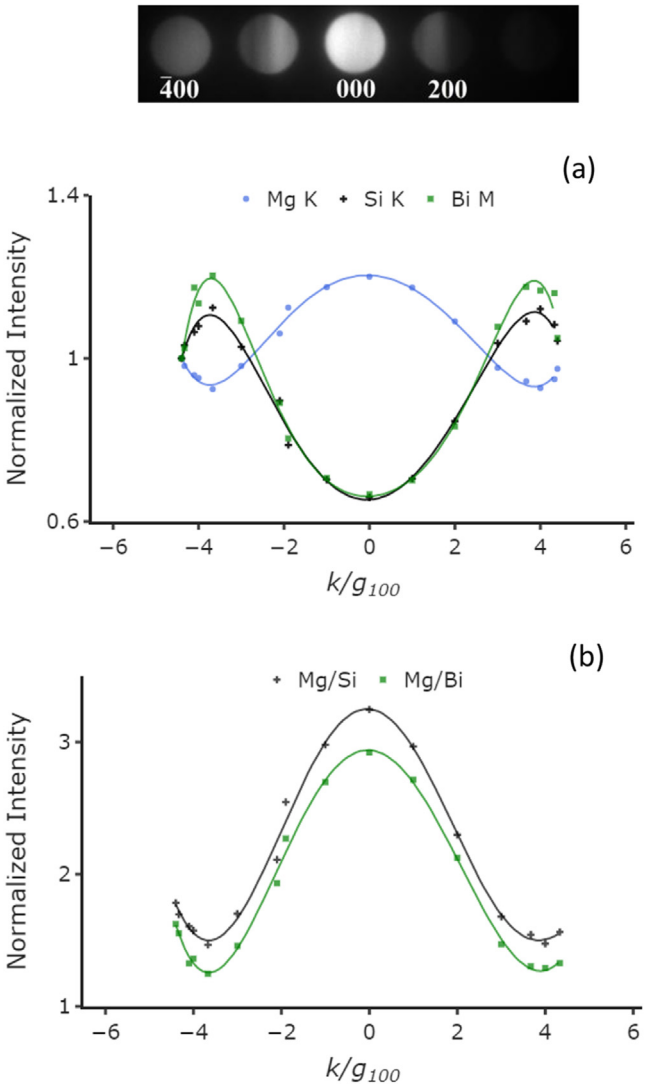

Fig. 5. (a) Normalized X-ray intensities for Mg, Si and Bi along the {100} row. The corresponding CBED pattern is also depicted on top of the graph. (b) Ratios between Mg, Si and Bi for the {100} row.

electron beam and the {100} and {111} crystal planes is shown in 5(a) and 6(a), respectively. On top of each graph, the corresponding CBED patterns of the {100} and {111} rows of reflections, in symmetrical conditions, are also presented. In both cases, a profound channeling effect is readily observed. This is further illustrated by the ratios between Mg (tetrahedral sites) and Si or Bi (octahedral sites), in Figs. 5(b) and 6(b) for {100} and {111}, respectively.

For the case of {100} row, Fig. 5, the variation of the normalized X-ray intensities for Mg, Si and Bi is symmetrical, in general, in accordance with the Mg_2Si structure symmetry. Furthermore, the Si and Bi curves follow the same trend and are always complementary to the Mg curve, which confirms the distinct site location for the three ions, i.e., octahedral for Si and Bi and tetrahedral for Mg [6].

The channeling results for the {111} row provide additional information. The Si and Bi curves are again complementary to Mg one, but all three become now asymmetrical as the electron beam varies along the {111} series of planes. The trend of the Mg curve confirms, on one hand, its location predominately in T (8c) sites; however, the asymmetry observed, in particular around the {222} reflections, implies some variable Mg content in its atomic positions. Vacancies generated by the Mg deficiency, generally observed by EDS point analysis, may well pro-

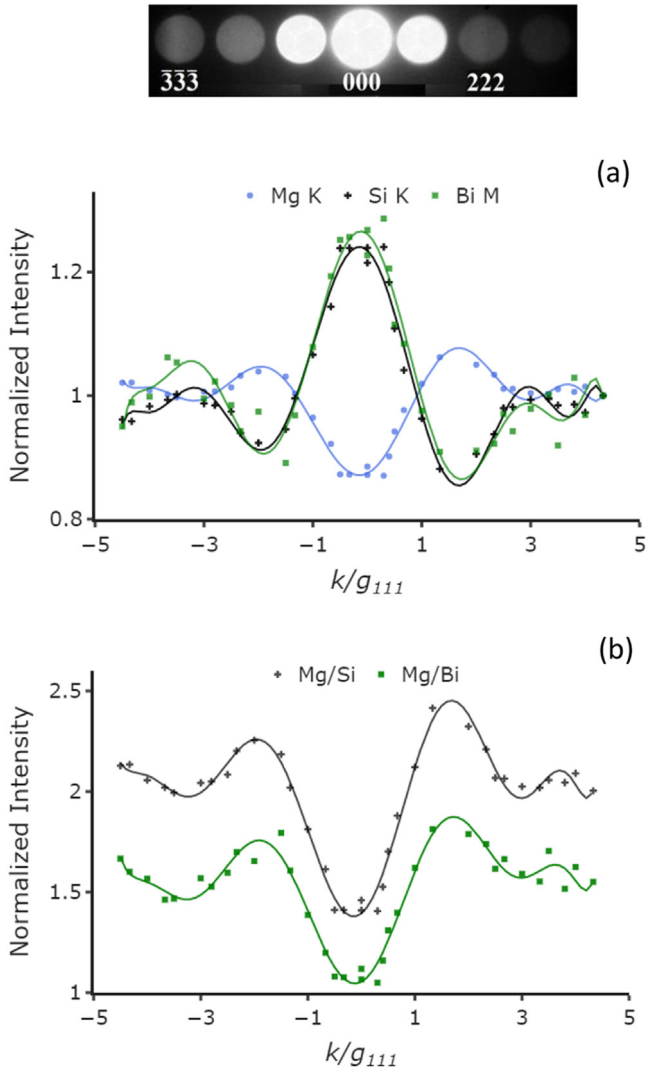

Fig. 6. (a) Normalized X-ray intensities for Mg, Si and Bi along the {111} row, along with its corresponding CBED pattern, on top of the graph. (b) Ratios between Mg, Si and Bi for the {111} row.

vide an explanation for these observations. Mg incorporation in other locations, too, such as interstitials in N (4b) sites, as in [26] can also be considered.

Furthermore, there are certain deviations from symmetry and complementarity for Bi, which may imply its location in different positions in the lattice, i.e., uneven Bi distribution. This is more pronounced in Fig. 6, along {111}, where the C and N sites are entirely distinguished, and the effect of uneven Bi distribution is stronger, especially around the {222} reflections. However, effects such as diffuse scattering from the incident and diffracted beams. i.e., absorption, or thickness variations due to imperfect shape of the areas analyzed may also cause variations in the shape of the channeling experimental curves [2,29]. Attempts, therefore, to minimize these effects took place, whenever feasible, such as choosing thin regions at the edge of Mg_2Si particles, as Fig. 3 illustrates, appropriately aligned with respect to the EDS detector. Moreover, contributions by additional reflections present during a series of channeling experiment, apart from the excited ones, may also induce inaccuracies in the results. A careful choice of the area analyzed, as well as the tilting conditions would be the remedy to overcome the latter obstacle.

By application of the ALCHEMI technique [28] the Bi content at each one of the Mg and Si sites can be calculated. The methodology is to choose two EDS spectra, one under strong channeling conditions (i.e., symmetric position) and one under uniform conditions, when the channeling effect is worn out (i.e., far away from all reflections in a reciprocal lattice row). The methodology assumes that there are three elements A, B and X, where element A occupies site 1, element B site 2 and element X is distributed between site 1 and 2. If the concentrations, as derived by the integration of their X-ray intensity peaks at the EDS spectra, of elements A (site 1) element B (site 2) and X are $N_A{}^c$, $N_B{}^c$ and $N_X{}^c$ under channeling and $N_A{}^u$, $N_B{}^u$ and $N_X{}^u$ under uniform conditions, the fraction c_X of the element X at site 1 (element A) would be

$$c_X = \frac{\left(N^c_X/N^u_X\right) - \left(N^c_B/N^u_B\right)}{\left(N^c_A/N^u_A\right) - \left(N^c_B/N^u_B\right)} \tag{8}$$

The criteria that the above calculations of c_X is accurate depend on the ratios $R(X/B)^{c,u}$, $R(X/A)^{c,u}$ and $R(B/A)^{c,u}$ (R factors), defined as follows:

$$R\left(X/B\right)^{c.u} = \frac{N^c_X/N^c_B}{N^u_X/N^u_B} \tag{9}$$

$$R\left(X/A\right)^{c.u} = \frac{N^c_X/N^c_A}{N^u_X/N^u_A} \tag{10}$$

$$R\left(B/A\right)^{c.u} = \frac{N^c_B/N^c_A}{N^u_B/N^u_A} \tag{11}$$

When $R(X/B)^{c,u} = 1$ and, simultaneously, $R(X/A)^{c,u} \neq 1$ and $R(B/A)^{c,u} \neq 1$, element X resides on site 2 (element B). The opposite takes place when $R(X/A)^{c,u} = 1$ and, simultaneously, $R(X/B)^{c,u} \neq 1$ and $R(B/A)^{c,u} \neq 1$, i.e., element X resides on site 1 (element A). Any differences in results due to delocalization of the effective interaction for inner shell ionization have not been considered here, as, among others, the study involves atoms with relatively higher atomic numbers [28,29].

In the current case, Mg, Si and Bi are elements A (site 1), B (site 2) and X, respectively. Application of Eqs. (8) to (11) for the {100} and {111} reciprocal rows yielded the results summarized in Table 2.

Table 2
Calculations of the Bi site preference for the pure Mg_2Si sample doped with Bi. In all cases, element 1/A is Mg, element 2/B is Si and element X is Bi.

Reciprocal row	c_X (%)	$R(X/B)^{c,u}$	$R(X/A)^{c,u}$	$R(B/A)^{c,u}$
{100}	1.4	1.011	0.555	0.549
{111}	−7.8	1.023	1.453	1.422

Regardless of the low concentration of Bi dopant in the sample, the results in Table 2 clearly confirm that the vast majority of Bi ions occupy Si octahedral sites. As deduced by the {100} row results, there is only 1.4% chance that Bi is located at Mg tetrahedral positions (T sites); furthermore, the outcome from the {111} row experiment leaves little doubt, as the amount of Bi occupying Si octahedral positions is 107.8%, i.e., due to the negative result in Table 2. In addition, these findings are in very good agreement with X-ray diffraction (XRD) analysis and TE properties measurements [16], where Bi incorporation brought upon both an increase of the host lattice constant and the n-type carrier concentration. Furthermore, there is a very good consistency of the values for the three criteria -Eqs. (9) to (11)- as in both {100} and {111} cases the $R(X/B)^{c,u}$ value is almost unity and both the $R(X/A)^{c,u}$ and $R(B/A)^{c,u}$ deviate strongly from 1. It is also noticeable that the deviations are towards the opposite sides of 1, i.e., much lower for {100} and much higher than 1 for the {111} series of channeling experiments, in line with the trend of the Mg, Si and Bi curves at Figs. 5(a) and 6(a), respectively.

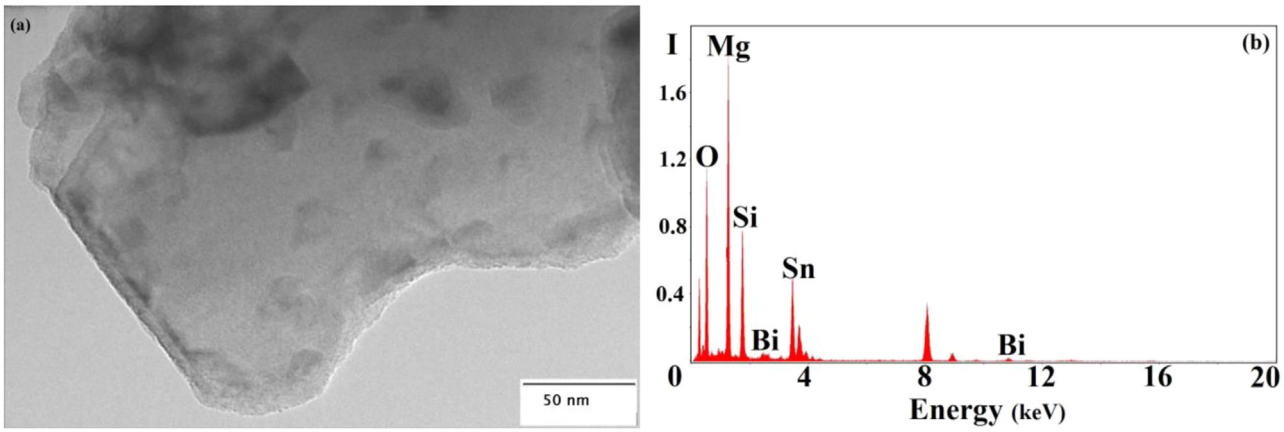

Fig. 7. (a) BF image from the edge of a typical particle for channeling at the Si-rich mixed $Mg_2Si_{1-x}Sn_x$ sample, (b) EDS spectrum from the sample.

3.2. Mixed $Mg_2Si_{1-x}Sn_x$ samples, doped with Bi

A characteristic BF image from a region analyzed in the Si-rich mixed $Mg_2Si_{1-x}Sn_x$ material is depicted at Fig. 7(a). In the case of mixed $Mg_2Si_{1-x}Sn_x$, phase separation is known to occur [15], so mixed Mg silicides often contain Si-, Sn-, Ge-rich particles and the so called 'matrix' phase, where the Si and Sn are almost at the same percentage (50 at%). Fig. 7(a) comes from a Si-rich particle. TEM/HRTEM observations did not show any extensive concentration of line or planar structural defects, a trend that was observed in the pure Mg_2Si, too.

An EDS spectrum from the Si-rich mixed $Mg_2Si_{1-x}Sn_x$ is shown in Fig. 7(b), where the peaks of Mg, Si, Sn and Bi are all shown, along with the O one (MgO phase). By obtaining several EDS spectra from distinct areas in the particle of 7(a), the consistency in the Mg, Si, Sn and Bi contents at the same particle is once more confirmed. However, there are often deviations from stoichiometry among different particles, due to the phase separation, as well as a small deficiency of Mg, towards an MgO formation [15,16], as in pure Mg_2Si.

Electron channeling experiments have been performed both along the {100} and {111} series of reflections. Due to the phase multiplicity in $Mg_2Si_{1-x}Sn_x$, we aimed to check the host and dopant ion distribution in both Si-rich and Sn-rich phases, therefore the channeling experiments along {100} and {111} were performed on several Si-rich and Sn-rich distinct particles, respectively.

The variation of the normalized X-ray emission versus the tilting angle for the {100} series for a Si-rich particle at the Si-rich mixed $Mg_2Si_{1-x}Sn_x$ sample is presented in Fig. 8.

In this case, the channeling effect is clearly observed, too, as further illustrated by the ratios between Mg (nominally tetrahedral) and Si, Sn or Bi (nominally octahedral), in Fig. 8(b). The curves in the mixed silicide, though, show significant deviations from symmetry, contrary to their respective symmetrical curves of Fig. 5, for pure Mg_2Si. In Fig. 8(a), the Si curve is always complementary to Mg one, whereas the Sn and Bi curves usually follow the Si curve trend, but not exclusively, especially around the {400} reflections. This trend shows that Bi dopant is mainly associated with Sn sites. Furthermore, the variation of X-ray emission for Bi (and Sn) is considerably asymmetric compared to the pure Mg_2Si case, Fig. 5(a).

The {111} row channeling experiments further confirmed the above findings. Following this, the X-ray intensity variation as a function of the angle between the incident electron beam and the {111} crystal planes is presented at Fig. 9. The EDS spectra now come from a Sn-rich particle at the Sn-rich mixed $Mg_2Si_{1-x}Sn_x$ sample, for reasons of comparison at the mixed $Mg_2Si_{1-x}Sn_x$ system. Here, the curves for Sn and Si are consistent and complementary to the Mg one, whereas Bi shows a more complex behavior. For Sn-rich particles, random Mg vacancies are more favoured than in Si-rich ones [27]; this has been also reflected in the Mg curve,

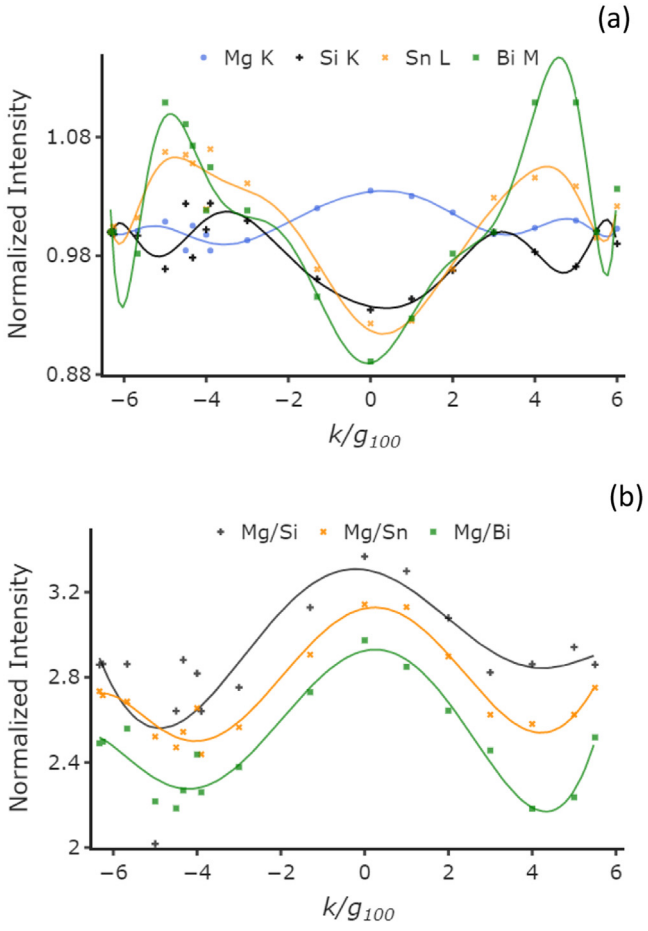

Fig. 8. (a) Normalized X-ray intensities for Mg, Si, Sn and Bi along the {100} row from a Si-rich particle at the Si-rich sample. (b) Mg/Si, Mg/Sn and Mg/Bi ratios for the same row of reflections.

which exhibits a certain level of asymmetry. As a consequence of the {111} planes effectively distinguishing the two octahedral sites (C and N), the asymmetry observed for Si, Sn and Bi shows that these elements do not exclusively occupy a specific octahedral site (C or N) but are randomly distributed in these two sites. Furthermore, this deviation from symmetry is more significant for Bi, which confirms its variable occupancy at the $Mg_2Si_{1-x}Sn_x$ crystal. The deviation is much larger compared

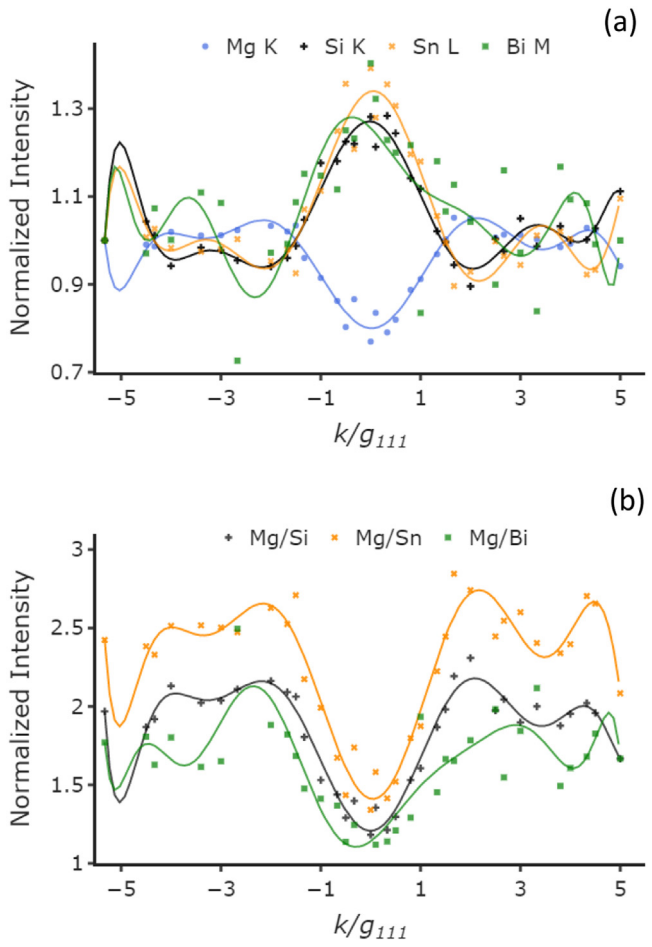

Fig. 9. (a) Normalized X-ray intensities for Mg, Si, Sn and Bi along the {111} systematic row of reflections from a Sn-rich particle at the Sn-rich mixed sample. (b) Mg/Si, Mg/Sn and Mg/Bi ratios for the same row of reflections.

Table 3
Calculations of the Bi site preference for the Si-rich mixed $Mg_2Si_{1-x}Sn_x$ sample doped with Bi. In all cases, element 1/A is Mg, element 2/B is either Si or Sn and element X is Bi.

	Reciprocal row	{100} Bi(Si)	Bi(Sn)
Si-rich	c_X (%)	−7.6	−25.4
	$R(X/B)^{c,u}$	0.986	0.962
	$R(X/A)^{c,u}$	0.836	0.836
	$R(B/A)^{c,u}$	0.849	0.870

to the Mg_2Si case -Fig. 6(a), as anticipated due to the mixed compound and unequal nominal Si and Sn contents.

The ratios between Mg (tetrahedral sites) and Si, Sn or Bi (octahedral sites) are also depicted in Fig. 9(b) for the {111} series, where we observe a strong channeling effect, too. The Bi curve profile, however, is again asymmetrical, due to its random distribution in the structure.

Application of ALCHEMI [28], Eqs. (8) to (11), has been performed for both the Si-rich and Sn-rich mixed samples, too and the results are presented in Tables 3 and 4, respectively.

In the mixed case samples, the Eqs. (8) to (11) may apply for all possible combinations of elements in positions 1/A and 2/B, i.e., Mg, Si or Sn. We chose to keep element 1/A as Mg and element 2/B as Si or Sn, whereas Bi is always element X. The Bi(Si) or Bi(Sn) columns in Table 3 and Table 4 refer to the case where element 2/B has been either Si or Sn, respectively.

Table 4
Calculations of the Bi site preference for the Sn-rich mixed $Mg_2Si_{1-x}Sn_x$ sample doped with Bi. In all cases, element 1/A is Mg, element 2/B is either Si or Sn and element X is Bi.

	Reciprocal row	{111} Bi(Si)	Bi(Sn)
Sn-rich	c_X (%)	−23.8	−1.84
	$R(X/B)^{c,u}$	1.095	1.008
	$R(X/A)^{c,u}$	1.823	1.823
	$R(B/A)^{c,u}$	1.665	1.808

In this case, the results are a little bit more complicated and are heavily dependent on the accuracy of the channeling experiments. Because of this, the results for the {111} series bear a greater significance, as their R values are more accurate. There is a general trend that Bi occupies sites of the majority element (Si in Si-rich, Sn in Sn-rich); however, Bi ions have a tendency to occupy sites related to Sn, as the R factors for the Sn-rich particle Table 4) are more accurate. This is complemented if we also choose, in addition, a further set of element positions: element 1/A is Sn, element 2/B is Si and element X is, again, Bi. In that case, Eqs. (8) to ((11) give:

c_X (%) = 110.34
$R(X/B)^{c,u}$ = 1.095
$R(X/A)^{c,u}$ = 1.008
$R(B/A)^{c,u}$ = 0.921

These results indicate that even more than 100% Bi ions are located at Sn sites, compared to Si ones, irrespective of the similar values of the R-factors; consequently, Bi ions show a preference to substitute for Sn sites in mixed $Mg_2Si_{1-x}Sn_x$ TE compounds. This aligns very well with previous electron microscopy and XRD findings [15,16], where Bi doping brought upon both an increase in the lattice constant and an enhancement of the phase separation, i.e., more Bi-doped Sn-rich particles.

Furthermore, the electron channeling findings and the ALCHEMI calculations confirmed the random distribution of Bi among the Si and Sn sites, as well as their own random order in the $Mg_2Si_{1-x}Sn_x$ crystallites. This is in very good agreement with the TE property measurements [16]. Among them, the electron carrier concentration and the electrical conductivity showed more than two orders of magnitude increase with 2–2.5 at% Bi doping, reaching ~3 10^{20} cm^{-3} and ~1750 Scm^{-1}, respectively. The Seebeck coefficient is also negative and decreases remarkably by more than 75% for 2–2.5 at% Bi [16]. These may well be explained by the Bi^{5-} substitution for Si^{4-}/Sn^{4-} sites.

A reduction in the lattice thermal conductivity component has been also observed [16], due to scattering of short-wavelength phonons by the point defects in the lattice created by the random distribution of both Bi dopants and, predominately, by the random distribution of host ions - Sn and Si, as this study showed. Thus, Si, Sn and Bi are all associated with both C and N sites. Furthermore, it has to be emphasized that, among the materials analyzed in this study, a compositional uniformity has been observed at all scale levels, from nano- (TEM) to micro- and macro-scale (EDS analysis in a Scanning Electron Microscope -SEM [15]), therefore there is a direct comparison between the electron channeling results and the TE properties.

4. Conclusions

Electron channeling and the ALCHEMI method has been employed to determine the location and distribution of both the host and dopant ions in magnesium silicide TE materials, doped with Bi. The study revealed that Mg ions occupy both tetrahedral T (8c) sites, $(\frac{1}{4}, \frac{1}{4}, \frac{1}{4})$ and $(\frac{1}{4}, \frac{1}{4}, \frac{3}{4})$, with some vacancies present, too, whereas Si, Sn and Bi occupy both 4a (C) and 4b (N) octahedral sites. In pure Mg_2Si, Si and Bi are intermixed between the pre-occupied 4a (0, 0, 0) C sites and the vacant, in

principle, 4b ($\frac{1}{2}$, $\frac{1}{2}$, $\frac{1}{2}$) N site. A random distribution in Bi ions has been observed. For the mixed $Mg_2Si_{1-x}Sn_x$ materials, the distinction between the tetrahedral 8c and octahedral 4a and 4b sites is still preserved, in relation to ion occupancy. However, although there is still an intermixing of Si, Sn and Bi ions in both 4a and 4b octahedral sites, there is a larger asymmetry of Bi in this case, which imply more random distribution in the mixed compounds. A tendency for Bi to substitute for Sn has been also detected. These findings are in very good agreement with the TE properties of the magnesium silicide materials, in terms of carrier concentration and electrical conductivity increase, negative Seebeck coefficient absolute decrease and lattice thermal conductivity reduction, due to random distribution of Si/Sn, as well as Bi incorporation in the host lattice instead of exclusive segregation at grain boundaries.

Declaration of Competing Interest

The authors declare that they have no known competing financial interests or personal relationships that could have appeared to influence the work reported in this paper.

CRediT authorship contribution statement

Andreas Delimitis: Conceptualization, Methodology, Formal analysis, Investigation, Visualization, Writing – original draft. **Theodora Kyratsi:** Investigation, Writing – review & editing. **Vidar Hansen:** Conceptualization, Methodology, Formal analysis, Funding acquisition, Investigation, Project administration, Resources, Supervision, Writing – review & editing.

Acknowledgments

The authors gratefully acknowledge the contributions of Johan Taftø, University of Oslo, in terms of experimental acquisitions and fruitful discussions, Elli Symeou for sample preparation and TE properties measurements and George Traskas, for fitting of the experimental data using Python.

References

[1] J. Taftø, Channeling effects in electron induced x-ray emission from diatomic crystals, Z. Naturforsch. 34a (1979) 452–458.
[2] J. Taftø, Z. Liliental, Studies of the cation atom distribution in $ZnCr_xFe_{2-x}O_4$ spinels using the channeling effect in electron-induced X-ray emission, J. Appl. Cryst. 15 (1982) 260–265.
[3] P.B. Hirsch, A. Howie, M.J. Whelan, On the production of X-rays in thin metal foils, Philos. Mag. 7 (1962) 2095–2100.
[4] G. Tan, F. Shi, S. Hao, L.D. Zhao, H. Chi, X. Zhang, C. Uher, C. Wolverton, V.P. Dravid, M.G. Kanatzidis, Non-equilibrium processing leads to record high thermoelectric figure of merit in PbTe–SrTe, Nat. Commun. 7 (2016) 12167.
[5] V. Hansen, C. Echevarria-Bonet, M. Wetrhus Minde, J. Taftø, Determination of atomic positions and polar direction in half-Heusler material $Sb_{1-x}Sn_xTi_{1-y-z}Hf_yZr_zCo$ using electron channeling, AIP Adv. 8 (2018) 125335.
[6] T. Morimura, M. Hasaka, ALCHEMI for coexistent Heusler and half-Heusler phases in $TiNi_{1.5}Sn$, Ultramicroscopy 106 (2006) 553–560.
[7] T. Zilber, S. Cohen, D. Fuks, Y. Gelbstein, TiNiSn half-Heusler crystals grown from metallic flux for thermoelectric applications, J. Alloys. Compd. 781 (2019) 1132–1138.
[8] B. Dado, Y. Gelbstein, M.P. Dariel, Nucleation of nano-size particles following the spinodal decomposition in the pseudo-ternary $Ge_{0.6}Sn_{0.1}Pb_{0.3}Te$ compound, Scr. Mater. 62 (2) (2010) 89–92.
[9] Y. Sadia, M. Elegrably, O. Ben-Nun, Y. Marciano, Gelbstein Y, Sub-micron features in higher manganese silicide, J. Nanomater. (2013) 701268.
[10] O. Meroz, Y. Gelbstein, Thermoelectric $Bi_2Te_{3-x}Se_x$ alloys for efficient thermal to electrical energy conversion, Phys. Chem. Chem. Phys. 20 (6) (2018) 4092–4099.
[11] Z.H. Zheng, D.L. Zhang, B. Jabar, T.B. Chen, M. Nisar, Y.F. Chen, F. Li, S. Chen, G.X. Liang, X.H. Zhang, P. Fan, Y.X. Chen, Mater. Today Phys. 24 (2022) 100659.
[12] C. Zhou, Y.K. Lee, Y. Yu, S. Byun, Z.Z. Luo, H. Lee, B. Ge, Y.L. Lee, X. Chen, J.Y. Lee, O. Cojocaru-Mirédin, H. Chang, J. Im, S.P. Cho, M. Wuttig, V.P. Dravid, M.G. Kanatzidis, I. Chung, Nat. Mater. 20 (2021) 1378–1384.
[13] M.N. Guzik, C. Echevarria-Bonet, M.D. Riktor, P.A. Carvalho, A.E. Gunnæs, M.H. Sørby, B.C. Hauback, Half-Heusler phase formation and Ni atom distribution in M-Ni-Sn (M= Hf, Ti, Zr) systems, Acta Mater. 148 (2018) 216–224.
[14] S. LeBlanc, S.K. Yee, M.L. Scullin, C. Dames, K.E. Goodson, Material and manufacturing cost considerations for thermoelectrics, Renew. Sustain. Energy Rev. 32 (2014) 313–327.
[15] G.S. Polymeris, N. Vlachos, A.U. Khan, E. Hatzikraniotis, C.B. Lioutas, A. Delimitis, E. Pavlidou, K.M. Paraskevopoulos, T. Kyratsi, Nanostructure and doping stimulated phase separation in high ZT $Mg_2Si_{0.55}Sn_{0.4}Ge_{0.05}$ compounds, Acta Mater. 83 (2015) 285–293.
[16] A.U. Khan, N.V. Vlachos, E. Hatzikraniotis, G.S. Polymeris, C.B. Lioutas, E.C. Stefanaki, M.K. Paraskevopoulos, I. Giapintzakis, T. Kyratsi, Thermoelectric properties of highly efficient Bi-doped $Mg_2Si_{1-x-y}Sn_xGe_y$ materials, Acta. Mater. 77 (2014) 43–53.
[17] M.I. Fedorov, V.K. Zaĭtsev, I.S. Eremin, E.A. Gurieva, A.T. Burkov, P.P. Konstantinov, M.V. Vedernikov, A.Y. Samunin, G.N. Isachenko, A.A. Shabaldin, Transport properties of $Mg_2X_{0.4}Sn_{0.6}$ solid solutions (X=Si, Ge) with p-type conductivity, Phys. Solid State 48 (8) (2006) 1486–1490.
[18] N. Vlachos, G.S. Polymeris, M. Manoli, E. Hatzikraniotis, A.U. Khan, C.B. Lioutas, E.C. Stefanaki, E. Pavlidouc, K.M. Paraskevopoulos, J. Giapintzakis, T. Kyratsi, Effect of antimony-doping and germanium on the highly efficient thermoelectric Si-rich-Mg_2(Si,Sn,Ge) materials, J. Alloys Compd. 714 (2017) 502–513.
[19] W. Fan, S. Chen, B. Zeng, Q. Zhang, Q. Meng, W. Wang, Z.A. Munir, Enhancing the zT value of Bi-doped $Mg_2Si_{0.6}Sn_{0.4}$ materials through reduction of bipolar thermal conductivity, ACS Appl. Mater. Interfaces 9 (2017) 28635–28641.
[20] P. Vivekanandhan, R. Murugasami, S. Kumaran, Rapid *in-situ* synthesis of nanocrystalline magnesium silicide thermo-electric compound by spark plasma sintering, Mater. Lett. 197 (2017) 106–110.
[21] A.Y. Samunin, V.K. Zaitsev, D.A. Pshenay-Severin, P.P. Konstantinov, G.N. Isachenko, M.I. Fedorov, S.V. Novikov, Thermoelectric properties of n–Type Mg_2Si–Mg_2Sn solid solutions with different grain sizes, Phys. Solid State 58 (8) (2016) 1528–1531.
[22] W. Liu, X. Tang, H. Li, K. Yin, J. Sharp, X. Zhou, C. Uher, Enhanced thermoelectric properties of n-type $Mg_{2.16}(Si_{0.4}Sn_{0.6})_{1-y}Sb_y$ due to nano-sized Sn-rich precipitates and an optimized electron concentration, J. Mater. Chem. 22 (2012) 13653–13661.
[23] J. Xina, H. Wub, X. Liua, T. Zhua, G. Yua, X. Zhao, Mg vacancy and dislocation strains as strong phonon scatterers in $Mg_2Si_{1-x}Sb_x$ thermoelectric materials, Nano Energy 34 (2017) 428–436.
[24] G. Jiang, J. He, T. Zhu, C. Fu, X. Liu, L. Hu, X. Zhao, High performance Mg_2(Si,Sn) solid solutions: a point defect chemistry approach to enhancing thermoelectric properties, Adv. Funct. Mater. 24 (2014) 3776–3781.
[25] N. Hirayama, T. Iida, K. Nishio, Y. Kogo, K. Takarabe, N. Hamada, Influence of native defects on structural and electronic properties of magnesium silicide, Jpn. J. Appl. Phys. 56 (2017) 05DC05.
[26] O. Jankaa, J.V. Zaikina, S.K. Bux, H. Tabatabaifar, H. Yang, N.D. Browning, S.M. Kauzlarich, Microstructure investigations of Yb- and Bi-doped Mg_2Si prepared from metal hydrides for thermoelectric applications, J. Solid State Chem. 245 (2017) 152–159.
[27] P. Zwolenski, J. Tobola, S. Kaprzyk, KKR–CPA study of electronic structure and relative stability of Mg_2X (X=Si, Ge, Sn) thermoelectrics containing point defects, J. Alloys Compd. 627 (2015) 85–90.
[28] J. Taftø, Electron channeling, structure factor phases, polarity and atom site determination in crystals, Micron 34 (2003) 157–166.
[29] J. Taftø, Structure-factor phase information from two-beam electron diffraction, Phys. Rev. Lett. 51 (8) (1983) 654–657.